Synchrotron X-ray refraction detects microstructure and porosity evolution during *in-situ* heat treatments

Itziar Serrano-Munoz [a,*], Ilaria Roveda [a], Andreas Kupsch [a], Bernd R. Müller [a], Giovanni Bruno [a,b]

[a] *Bundesanstalt für Materialforschung und -prüfung (BAM), Unter den Eichen 87, 12205, Berlin, Germany*
[b] *University of Potsdam, Institute of Physics and Astronomy, Karl-Liebknecht-Str. 24-25, 14476, Potsdam, Germany*

ARTICLE INFO

ABSTRACT

For the first time, synchrotron X-ray refraction radiography (SXRR) has been paired with *in-situ* heat treatment to monitor microstructure and porosity evolution as a function of temperature. The investigated material was a laser powder bed fusion (LPBF) manufactured AlSi10Mg, where the initial eutectic Si network is known to disintegrate and spheroidize into larger particles with increasing temperature. Such alloy is also prone to thermally induced porosity (TIP). We show that SXRR allows detecting the changes in the Si-phase morphology upon heating, while this is currently possible only using scanning electron microscopy. SXRR also allows observing the growth of pores, usually studied via X-ray computed tomography, but on much smaller fields-of-view. Our results show the great potential of *in-situ* SXRR as a tool to gain in-depth knowledge of the susceptibility of any material to thermally induced damage and/or microstructure evolution over statistically relevant volumes.

1. Introduction

Among the material characterization techniques, optical and electron microscopy provide detailed 2D spatially resolved information about the morphology and distribution of microstructural features present in bulk materials. Nonetheless, these techniques are frequently destructive and samples cannot be tested after analysis; moreover, sample preparation is elaborative and time consuming, and the investigation of features at the submicrometre scale is limited to very small fields-of-view (FoVs) [1]. In addition, laboratory [2,3] and synchrotron [4] X-ray computed tomography (XCT) allow a 3D non-destructive evaluation of defect populations and/or phase components. However, the imaging of microscopic features (say from 1 to 5 μm) requires miniature samples (1–2 mm diameter at most) in the case of classic synchrotron XCT. Enlarging the field of view (*e.g.*, to 10–20 mm) by using laboratory XCT comes at the cost of a reduced spatial resolution (>5 μm).

Complementarily, X-ray refraction methods [5–7] are radiographic and tomographic techniques that combine a macroscopic field-of-view (a few tens of mm^2) with an exceptional detectability of submicron features. Most commonly, X-ray refraction is used in radiographic mode using thin specimens (platelets) to obtain a so-called 2.5D signal (*i.e.*, integrated through the specimen thickness). Populations of submicron

defects can be detected rather than single defects imaged. The necessity of a certain population of interfaces is because the discontinuities present in the sample need to contribute a sufficient signal to yield an integrated intensity above the background noise. Synchrotron X-ray refraction radiography (SXRR) has been successfully used to detect submicron features (*e.g.*, microcracks, voids and second phase particles) in bulk materials such as ceramics [8,9], metals [10,11], and epoxy matrix composites [7,12]. Some of the studies report on the *evolution* of defects during *in-situ* tensile tests [11,12]. Recently, the use of SXRR was extended to categorize the void population in laser powder bed fusion (LPBF) manufactured TiAl6V4 and LPBF IN718 materials [13–15].

LPBF is an additive manufacturing (AM) technique that has experienced an exponential growth in the past decade for its unrivalled freedom of design. It allows the production of complex near-net shaped parts with improved functionalities [16]. In particular, Al-Si is one of the alloy systems more comprehensively investigated in the LPBF open literature due to its high demand for various applications in the aerospace and automotive industries [17]. Despite the myriad of advantages enabled by AM, these techniques typically induce defects (*e.g.*, gas porosity [4,18,19]) and layer-wise microstructure heterogeneity [20–22] in the as-built condition. Even in the case of optimized process parameters, which leads to the production of materials with high relative density (>99% [23,24]), voids can be formed due to the entrapment

---

of gases during the process [25,26], as well as to thermally induced porosity (TIP) during post-processing heat treatments [27–30].

The morphology and size of the eutectic silicon in Al-Si alloys largely determine the mechanical behaviour of fully dense materials, and consequently, much attention has been devoted to the optimization of heat treatments [31–34]. The high solidification rates characteristic of LPBF processing (10^4–10^6 °C/s) induces the formation of a nanometric silicon network within the α-Al matrix [34]. This combination leads as-built LPBF AlSi10Mg to exhibit higher yield strength than conventional cast materials. Not that baseplate preheating (at 150–200 °C) during manufacturing is effectively used to prevent cracks and minimize distortions [35]. Another strategy to avoid distortion is by performing a stress relief heat treatment (300 °C for 2 h) prior to the part removal from the baseplate. Afterwards, the material is subjected to solution heat treatments, usually performed at 500–550 °C for 1–2 h. These two heat-treatment schemes inevitably lead to the expulsion of solid solution silicon atoms from the α-Al matrix (down to 3-2%) and the disintegration of the silicon network into fine (in the case of treatments at about 300 °C) or blocky (in the case of treatments at 500–540 °C) Si particles. In both cases, the ripening of Si particles results in a decrease of the yield strength.

The complexity of any microstructural characterization significantly increases when there is a need to perform it as a function of temperature. To date, this characterization is primarily performed by undertaking labour-intensive *ex-situ* experiments interrupted at different temperatures or times. Moreover, these studies are often limited to a sample region smaller than the representative elementary volume. This limitation can lead to partial or even biased interpretations of the collected data. The scientific added value of developing alternative and complementary *in-situ* methods, which enable monitoring the metallurgical evolution of microstructures in engineering materials over large FoVs, is therefore obvious. The current study presents, for the first time, *in-situ* investigations of pore growth and microstructural evolution by means of SXRR. Complementarily, the studied LPBF AlSi10Mg material was also investigated by *ex-situ* microscopy, and laboratory and synchrotron XCT.

2. Materials and methods

2.1. Material manufacturing

The investigated material was produced at Deutsches Zentrum für Luft-und Raumfahrt (DLR) on a Concept Laser M2 machine. Gas atomised AlSi10Mg powder in the virgin state was used to manufacture 8 × 20 × 110 mm³ prisms under argon atmosphere. The height of the samples (110 mm) was parallel to the building direction (BD). The LPBF samples were built using a 30 μm layer thickness and a 380 W fibre laser set at a speed of 1500 mm/s. A hatching distance of 100 μm was employed. The chessboard scan strategy consisted of 5 × 5 mm² islands. The scan vectors were rotated 90° between adjacent islands and 45° between subsequent layers. In addition, there was a shift of the island locations between layers to avoid the superposition of the island borders along the BD. During the entire process, the building platform was kept at a temperature of 200 °C. The surface roughness was reduced using contour layers.

2.2. Microscopy

The microscopy specimens were polished using a series of SiC papers (1200, 2400 and 4000 grit) prior to the use of a 3 μm diamond slurry applied on a polishing cloth. The final polishing step required the use of colloidal silica suspension for a minimum of 3 min. The etching of the polished surfaces was performed using a Dix & Keller reagent (190 ml H_2O; 5 ml HNO_3; 10 ml HCl; 2 ml HF) for 15 min. The characterization of meso- and microstructures was conducted using a light optical microscope (POLYVAR MET, Reichert-Jung equipped with a Gryphax-Altair camera) and a field-emission gun scanning electron microscope (FEG-

SEM) LEO 1530VP (Zeiss, Germany). The SEM was operated at an acceleration voltage of 20 kV, a probe current of 7–8 nA in high pressure mode, and using a working distance of 9-8 mm. The secondary electron (SE) imaging mode was used. The equivalent circular diameter ($\text{Ø}_{eq} = 2*(A/\pi)^{1/2}$) of silicon particles as a function of heat treatment was determined using the image analysis software package Fiji™ [36].

2.3. X-ray computed tomography (XCT)

For the quantitative analysis of the porosity contained within the sample volume (*i.e.*, 8 × 20 × 20 mm³), XCT measurements were performed using a custom-built micro-XCT system equipped with a 225 kV X-ray source manufactured by X-ray WorX GmbH and a 2048 × 2048-pixel detector manufactured by PerkinElmer, Inc. The X-ray source settings during the scans were: 120 kV acceleration voltage and 120 μA tube current. A pre-filter of 0.5 mm thick copper was used to supress undesired low-energy X-rays and reduce the beam hardening effect, thereby improving the image quality. 2D projection images were collected at 3000 equally spaced rotation increments over 360°. The exposure time for each projection image was 6 s. The voxel size was $(14.5\ \mu m)^3$. The images were reconstructed using an in-house developed code.

The *ex-situ* XCT examination of thermally induced porosity (TIP) before and after the heat treatment (1 h at 540 °C) was performed using a v|tome|x L 300 XCT scanner from General Electric (GE). For the two scans, a voltage of 120 kV and a tube current of 60 μA were used, and the exposure time was set to 5 s for each of the 3000 projections over 360°. A Cu filter of 0.1 mm thickness was utilized. The images were reconstructed using the GE standard algorithm. To enable higher resolution (voxel size $(5.8\ \mu m)^3$), a coupon of 4.0 × 6.8 × 5.3 mm³ was extracted from the as-built sample.

A further analysis of porosity was performed at the P05 beamline of the PETRA III storage ring (DESY, Hamburg, Germany) [37]. The energy of the monochromatic beam was set at 20 keV, the distance between sample and detector was 70 mm, the number of projections was 1801 (over 180°), and the exposure time was 220 ms. A 1 mm diameter pin was used in combination with an effective voxel size (after 2 × binning) of $(1.28\ \mu m)^3$. The projections were reconstructed using the in-house routine available at P05.

Data processing was performed using the Avizo® software package [38]. For denoising, the raw data were filtered using a non-local mean filter. The pores were identified by global threshold segmentation. To reduce the probability of false segmentation due to image artefacts, only voids with a minimum size higher than 2 voxels were considered. The binarized images were subsequently used for the evaluation of volumetric parameters (i.e., the equivalent spherical diameter, $\text{Ø}_{eq} = (6*V/\pi)^{1/3}$, and the porosity volume fraction - referred to as area fraction in the case of 2D images).

2.4. X-ray refraction

X-ray refraction occurs whenever X-rays interact with interfaces between materials of different (electron) densities. The refraction angle depends both on the two interfacing materials and on the wavelength of the radiation. Since the standard X-ray wavelengths are around 0.1 nm, X-ray refraction occurs at very small scattering angles, in the order of some seconds to minutes of arc. X-ray refraction techniques are able to detect discontinuities as soon as their size exceeds a few X-ray wavelengths (*i.e.*, the wave interacts with the density difference at the interface). Thus, the smallest detectable object size is theoretically down to the nanometre range. Emphasis is given to the fact that "detectable" does not necessarily mean that the individual object can be imaged. As is the case in synchrotron XCT, the imaging capabilities are limited by the pixel size of the detector system. Surface roughness contributes to the refraction signal, so that platelets need to be polished down to 4000 SiC grit paper to prevent overlap between surface and volume features in the

X-ray refraction signal.

2.4.1. In-situ heating and X-ray refraction at the BAMline

A dismantled head of a decommissioned micro-focus X-ray tube of 62 mm diameter was repurposed to serve as dome (see Fig. 1a) of the furnace used for high-temperature measurements (an Anton Paar hot stage, DHS 1100 model). A pair of diametrically opposite Beryllium windows were used as beam entrance and exit. The anode material in the head of the tube had to be removed. The removed material was replaced by a 1 cm thick Aluminium lid. Prior to the experiment, it was verified that the Be windows caused negligible attenuation and refraction.

A mini holder (Ø = 12 mm × 4.5 mm dimensions, stainless steel 430) containing a minivise and a 4 mm slot was used to mount a 1 mm thick AlSi10Mg platelet onto the oven hot plate (Fig. 1b). The platelet was positioned with the building direction pointing upwards (i.e., parallel to the scattering vector). The temperature was measured by a thermo-couple located below the hot plate. The heating and cooling rates were set to 10 °C/min. The different steps investigated by in-situ SXRR are listed in Table 1. Note that the last stage (number 16), was measured after the heating was stopped and the sample cooled down (i.e., the cooling was achieved by thermal equilibration).

SXRR measurements were carried out at the BAMline (BESSY II synchrotron of the Helmholtz Zentrum Berlin (HZB), Germany) [7,39, 40]. A highly collimated monochromatic X-ray beam (with $\Delta E/E$ ~0.2%) was provided by a double crystal Si monochromator (DCM). The beam energy was set at 17.5 keV to obtain an X-ray transmission of about 30% through the 1 mm thick AlSi10Mg platelet. A pco.1600 camera (1600 × 1200 pixels) combined with a lens system and a 50 μm thick cadmium tungstate (CWO) scintillator screen enabled to reach a pixel size of 4.08 μm. In order to prevent detector backlighting [41,42], the incident beam was narrowed to the resulting FoV of ~ 6.3 × 4.7 mm^2 by a slit system. A Si(111) analyser single crystal was placed in the beam path between the specimen and the camera system to perform refraction radiographs according to the DEI (Diffraction Enhanced Imaging, also called ABI, Analyzer-Based Imaging) scheme [43] (see Fig. 1a).

The analyser crystal was aligned so that the (111) reflection (Bragg angle $\theta_B = 6.4876°$ at 17.5 keV) is recorded by the detector. Collecting radiographs at different tilt angles (symmetric to θ_B) of the analyser crystal allows recording the so-called rocking curve. Such curve describes the reflected beam intensity as a function of the deviation from the Bragg angle for each detector pixel (see Fig. 2, extracted from an arbitrary detector pixel). In the current study, 61 radiographs were recorded between $\theta = 6.4816°$ and 6.4936°, with a step size of $\Delta\theta = 0.0002°$ and exposure time of 1.5 s. The total acquisition time was 2–3 min at each temperature step. To properly evaluate the series of images, we had to record the flat field (beam on, no specimen) and the dark field

Table 1
List of the different temperature steps at which the microstructure and porosity evolution was monitored (SXRR measurements).

Step number	Temperature at the hot plate	Step number	Temperature at the hot plate
1	25 °C	9	300 °C, 1 h
2	170 °C	10	540 °C, 0 h
3	220 °C	11	540 °C, 0.5 h
4	265 °C, 0 h	12	540 °C, 1 h
5	265 °C, 0.5 h	13	650 °C, 0 h
6	265 °C, 1 h	14	650 °C, 0.5 h
7	300 °C, 0.5 h	15	650 °C, 1 h
8	300 °C, 0.5 h	16	25 °C
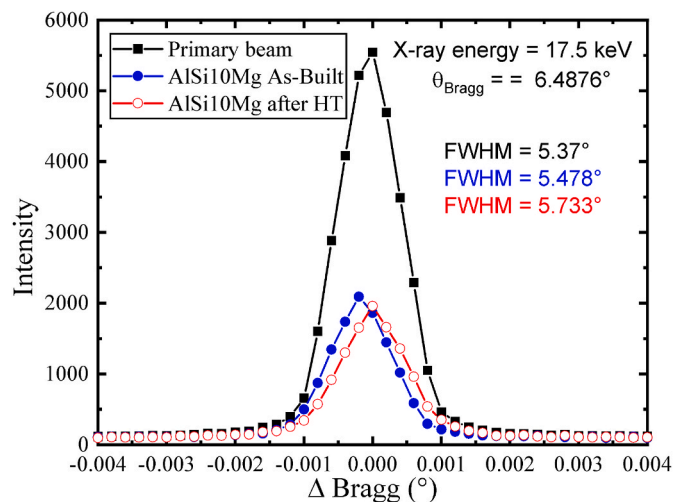
Fig. 2. Rocking curves measured at an arbitrary detector pixel. Squares: without sample in the beam. Filled circles: with sample in the beam for the as-built condition. Open circles: with sample in the beam at room temperature after the heat treatment cycle.

(beam off) images over the whole rocking curve (note that the sample environment had to remain mounted). Unfortunately, once mounted, the sample could not be moved off the beam-path separately from the furnace. This limited the number of flat fields to two (instead of 16, ideally corresponding to every temperature step), the first one recorded before the sample was mounted, and the second one recorded once the heat treatment was over and the sample was dismounted.
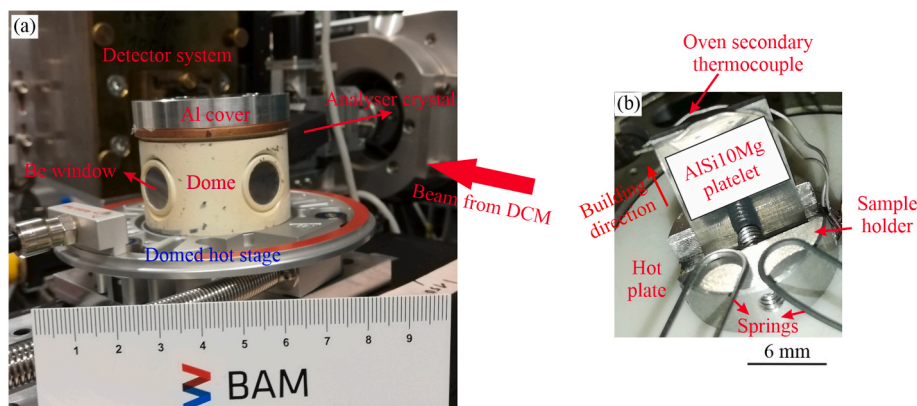
Fig. 1. (a) Photo of the X-ray refraction set-up at the BAMline showing the main components of the in-situ oven. (b) Detail of the interior of the dome, where the field-of-view is indicated with a white rectangle.

2.4.2. Data processing

The rocking curves were fitted using a pseudo-Voigt function. The fitting was performed using an in-house software code [44] programmed using Python™ [45]. The routine computes the values of the rocking curve integral, the peak height, the peak position and the full width at half maximum (FWHM). The attenuation ($\mu * d$) and the refraction value ($C_m * d$) were evaluated for each pixel according to Equations (1) and (2), respectively:

$$\mu * d = \ln\left(\frac{I_0}{I}\right) \tag{1}$$

$$C_m * d = 1 - \frac{I_R * I_0}{I_{R0} * I} \tag{2}$$

where I_0 is the peak integral (see Fig. 2) and I_{R0} the peak height without the specimen in the beam, I the peak integral and I_R the peak height with the specimen in the beam, and d is the sample thickness. For the derivation of equation (2) the reader is referred to Ref. [11]. All the quantities mentioned above are converted to greyscale images.

As shown in Fig. 2, a reduction in the peak integral intensity was observed once the AlSi10Mg platelet was in the beam (compare the primary beam rocking curve to those with the sample in the beam). This reduction is purely related to the absorption properties of the sample.
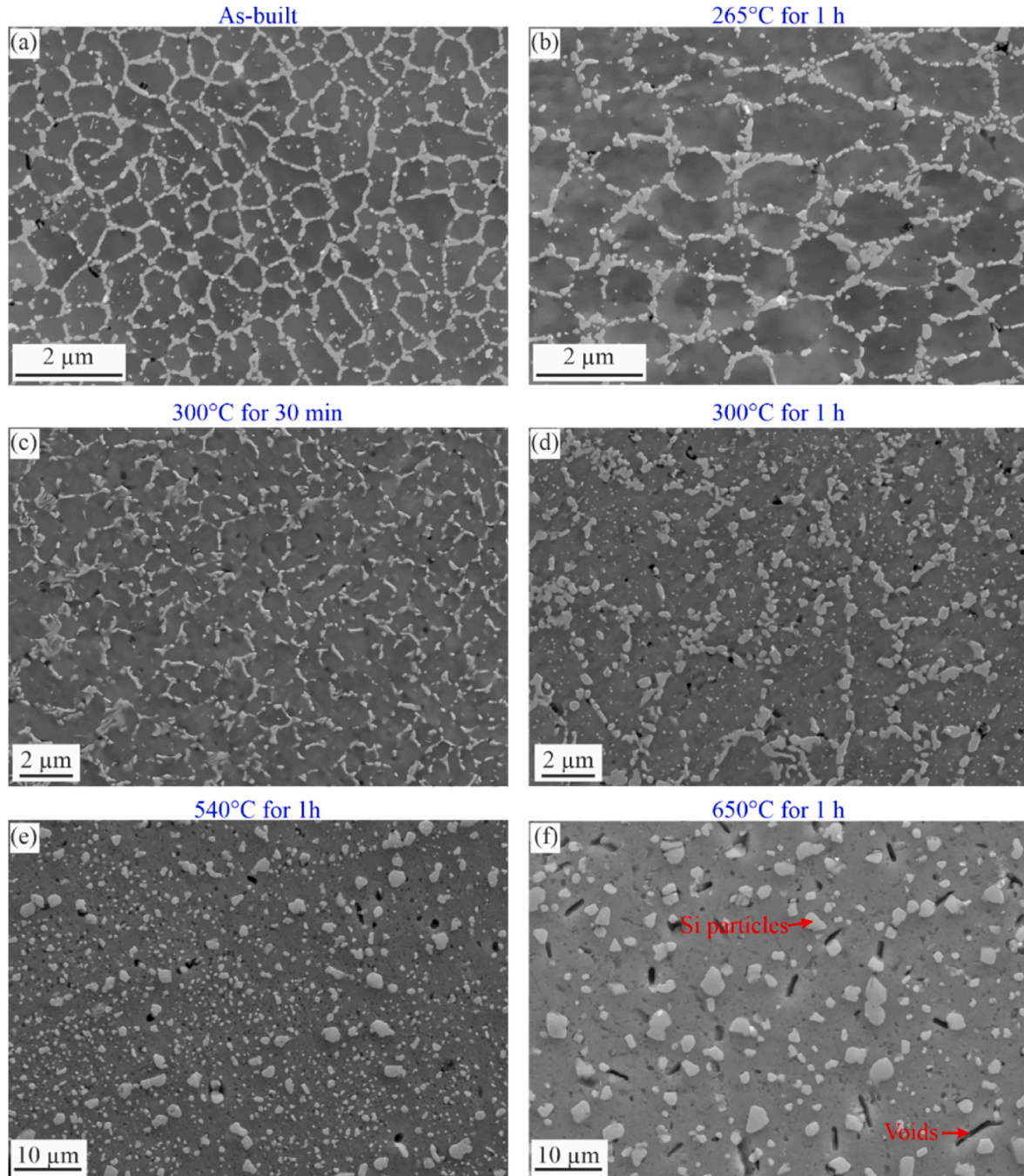
Fig. 3. SEM-SE images showing the AlSi10Mg microstructure (a) in the as-built condition, (b) after 1 h at 265 °C, (c) after 30 min at 300 °C, (d) after 1 h at 300 °C, (e) after 1 h at 540 °C, and (f) after 1 h at 650 °C (the voids correspond to detached Si particles or porosity). The α-Al matrix is shown in dark grey, the Si in lighter grey, and voids appear in black. Note that for the sake of clarity, the magnification changes between a-b, c-d, and e-f images (see scale bars).

Due to the thermally induced growth of the porosity population (*i.e.*, changes at the internal interfaces), we observed an increase in the width (FWHM) of the curve when comparing the post-heat-treated (Step 16) with the as-built (Step 1) condition.

For a quantitative evaluation of the results, we used the transmission (*i.e.*, ($\mu*d$)) and refraction (C_m*d) values. The first is proportional to the local density, while the latter is proportional to the (internal) specific surface (surface per unit volume). Beyond direct imaging of mesoscopic objects (such as pores extending over a few pixels), C_m*d allows the quantification of the population (frequency) of submicron structural defects with size below the spatial resolution of the detector system (4.08 μm). The quantitative evaluation of the transmission images was performed with a similar protocol as the one introduced in the last paragraph of section 2.3.

3. Results

3.1. Microstructure

The as-built condition (Fig. 3a) shows a thin nanometric Si network (70 nm thickness in average), which encloses the α-Al cells (0.7 μm average size) and is mostly interconnected. The Al cells contain fine Si precipitates (about Ø > 20 nm, according to Ref. [33]). After heat treatment at 265 °C for 1 h (Fig. 3b), the eutectic Si network becomes thicker (about 100 nm in average) and the α-Al cells larger (~1.2 μm). This enlargement relates to Si atoms being expelled from the supersaturated α-Al matrix and precipitating along the cells boundaries, followed by ripening (as also predicated in Ref. [33]).

After 30 min at 300 °C, the Si network is broken down and transformed (presumably by Al-Si interdiffusion [33]) into Si vermicular rods (Fig. 3c). A longer heat treatment (Fig. 3d), at 300 °C for 1 h, induces a globularization, resulting in polygonal Si particles homogeneously distributed in the α-Al matrix and possessing a wide size range (the average equivalent diameter is actually around 70 nm). This large size distribution is generally attributed to the fact that the larger particles are globularized from the initial Si network and the smaller ones develop from the initial fine intragranular Si precipitates [33]. As documented in some previous works [31,33], the size of Si particles increases after heat treatment at 540 °C for 1 h, and a bimodal distribution of the Si particle size is observed (average $\varnothing_{eq}$ = 300 nm, Fig. 3e). Finally, after 1 h at 650 °C, the size of Si particles is further increased ($\varnothing_{eq}$ = 600 nm, Fig. 3f).

3.2. Porosity analysis

The porosity mainly consists of *large* spherical pores (Type I, hereafter) homogeneously distributed all over the investigated height (Fig. 4a and b). These pores are associated to excessive volumetric energy densities (E_v) [18]. Examination of the perspective along the BD (Fig. 4c) indicates three preferential zones for Type I porosity formation: (i) *contour porosity* (*i.e.*, the porosity line observed along the perimeter in Fig. 4c) occurring within the contour scan regions and most likely resulting from low heat dissipation into the powder; (ii) *interface porosity* developing at the border between the contour and the bulk, due to the increased local energy density induced by the deceleration and acceleration of the laser beam during turning; and (iii) *island porosity* occurring at the boundaries between adjacent islands (creating a chessboard pattern), commonly induced by excessive overlap. In the visualized region, the pore volume fraction is 0.77% and the average equivalent spherical diameter is 50 μm.

The porosity distribution along the height is further examined using room temperature SXRR, which required the extraction of a 1 mm thick platelet. The X-ray refraction radiography image representing the peak position (Fig. 5a) also shows the presence of Type I (macroscopic) pores all over the investigated volume (note that the contour region is not included in the FoV). In addition, the refraction signal enables the
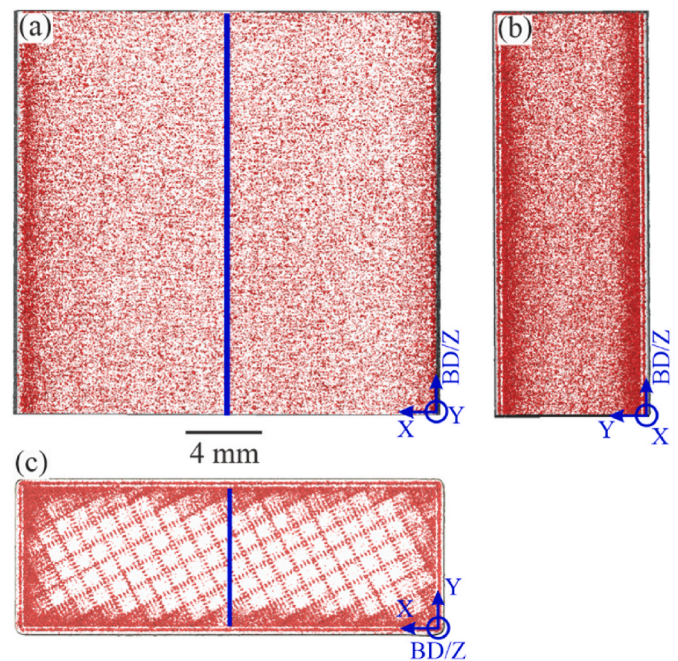

Fig. 4. 3D volume renderings obtained via loboratory X-ray CT (the aluminium matrix is made transparent) showing the (a) X-Z perspective where all the pores are projected along Y, (b) Y-Z perspective, where all the pores are projected along X, and (c) X–Y perspective, where all the pores are projected along Z. The location of the platelet extracted for SXRR measurements (see Fig. 5) is indicated with a blue line. (For interpretation of the references to colour in this figure legend, the reader is referred to the Web version of this article.)

visualization of smaller gas pores (called Type II, indicated with a blue arrow in Fig. 5b) that are below the detection limit of the data shown in Fig. 4. When comparing an optical microscopy image of one of the surfaces of the specimen (Fig. 5c) with the refraction radiography (*i.e.*, the C_m*d map shown in Fig. 5d), we observe that Type II pores are principally localized around the melt pool boundary between laser tracks and exhibit C_m*d values higher than 0.1. Instead, Type I create randomly distributed crescent-shaped features of similar C_m*d values (> 0.1). Type II porosity strongly clusters in the first chessboard columns (i. e., those adjacent to the contour) and progressively thins out in successive columns. From Fig. 5d, it is also visible that not all layers exhibit a noticeable localization.

Typically, the source of Type II porosity in powder AM is ascribed to the presence of pre-existing gas entrapped in the feedstock powder particles, as well as to the occurrence of vaporized material during fusion. In both cases, the gas is not able to escape from the melt pool [26]. In addition, aluminium attracts moisture, which is considered the main source of hydrogen porosity in LPBF aluminium materials: through an oxidation reaction between water vapor and the liquid Al, H^+ protons will be formed as by-product [18,25,28]. The formation of hydrogen porosity results from the reduced solubility of hydrogen in the solid state [30]. Fortunately, the rapid cooling rates (10^4–10^6 °C/s) induced by LPBF lead to considerable hydrogen supersaturation within the aluminium lattice. Such phenomenon has been reported to help reducing the amount of process-induced hydrogen porosity [25,46]. Furthermore, the preferential entrapment of porosity at the melt pool boundary has been ascribed to the development of walls of oxide films that reduce the wettability with the substrate, therefore inducing a localized formation of pores [47]. Another mechanism is proposed in Ref. [25]: the localization of pores at the melt pool boundary is induced by the hydrogen solubility gap between Al liquid and solid states.

Fig. 6 shows the high-resolution Synchrotron X-ray CT (SXCT) results, where the two types of porosity can be discriminated by their size. The evaluation of these data yields a volume fraction of 0.6% and an
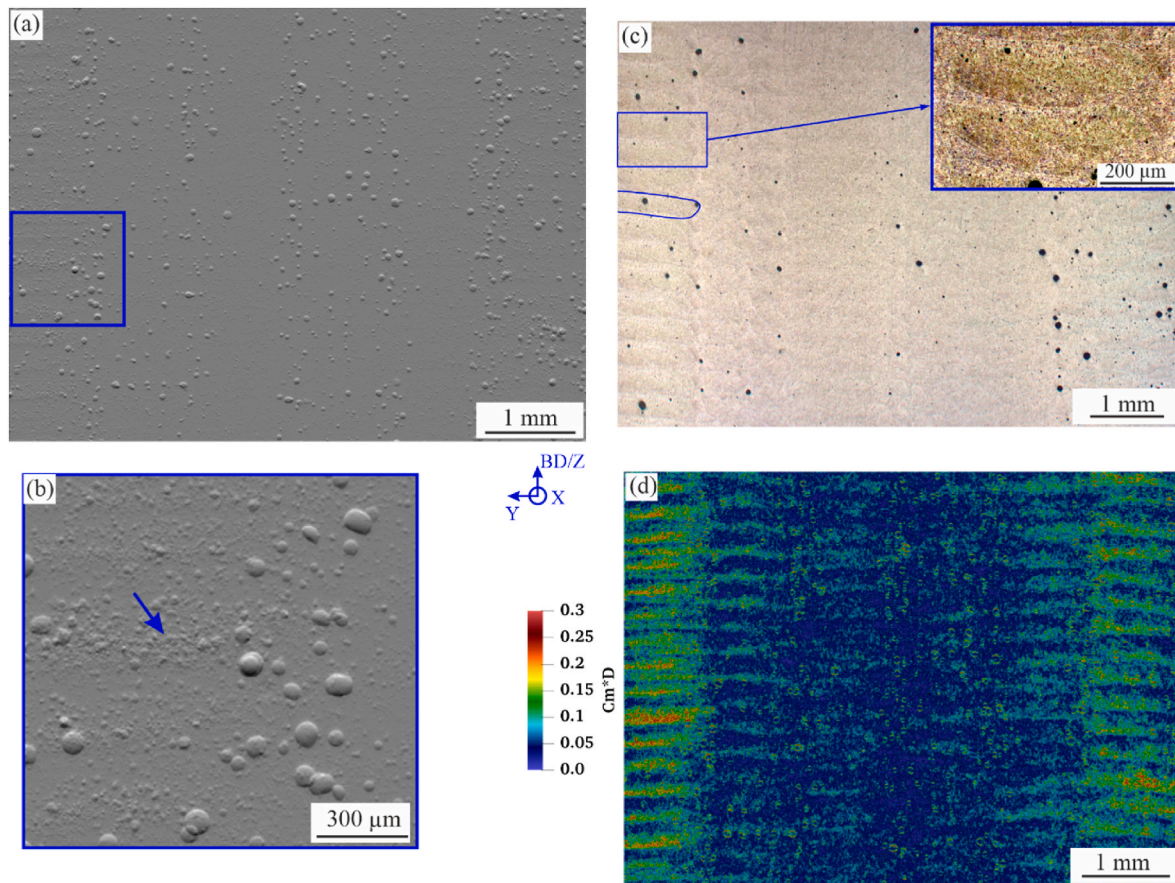
Fig. 5. (a) Synchrotron X-ray refraction radiography (SXRR) image of the AlSi10Mg platelet representing the peak position; the blue square indicates the location of the detail shown in (b). (c) Optical microscopy image showing the melt pool boundaries (an example is outlined in blue and in the inset) and porosity in black. (d) Colour-coded C_m*d refraction image highlighting the melt pool boundaries; it is to be noted that (c) contains information from the surface of the specimen, while (d) mainly contains information from the interior of the specimen. (For interpretation of the references to colour in this figure legend, the reader is referred to the Web version of this article.)
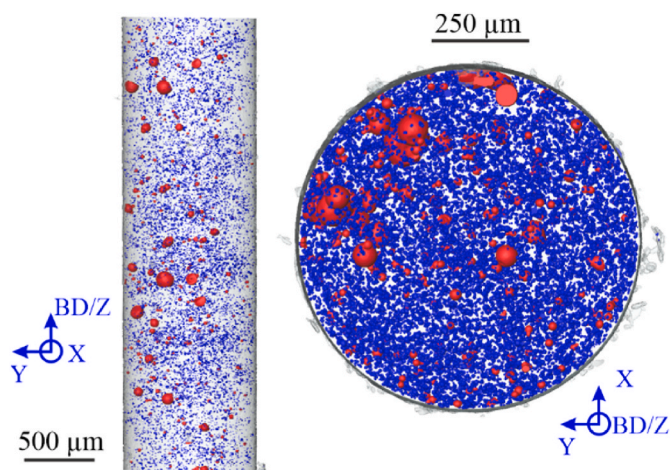
Fig. 6. 3D volume renderings obtained from SXCT data showing (a) Y-Z perspective and (b) X-Y perspective. Type I porosity is shown in red and Type II porosity in blue. (For interpretation of the references to colour in this figure legend, the reader is referred to the Web version of this article.)

average equivalent diameter of 5 μm, in the case of Type II porosity.

A 3D *ex-situ* evaluation of the increase of the pore size (thermally induced porosity, TIP) associated with heat treatment is shown in Fig. 7. The pore volume fraction grows from 0.48% in the as-built condition to
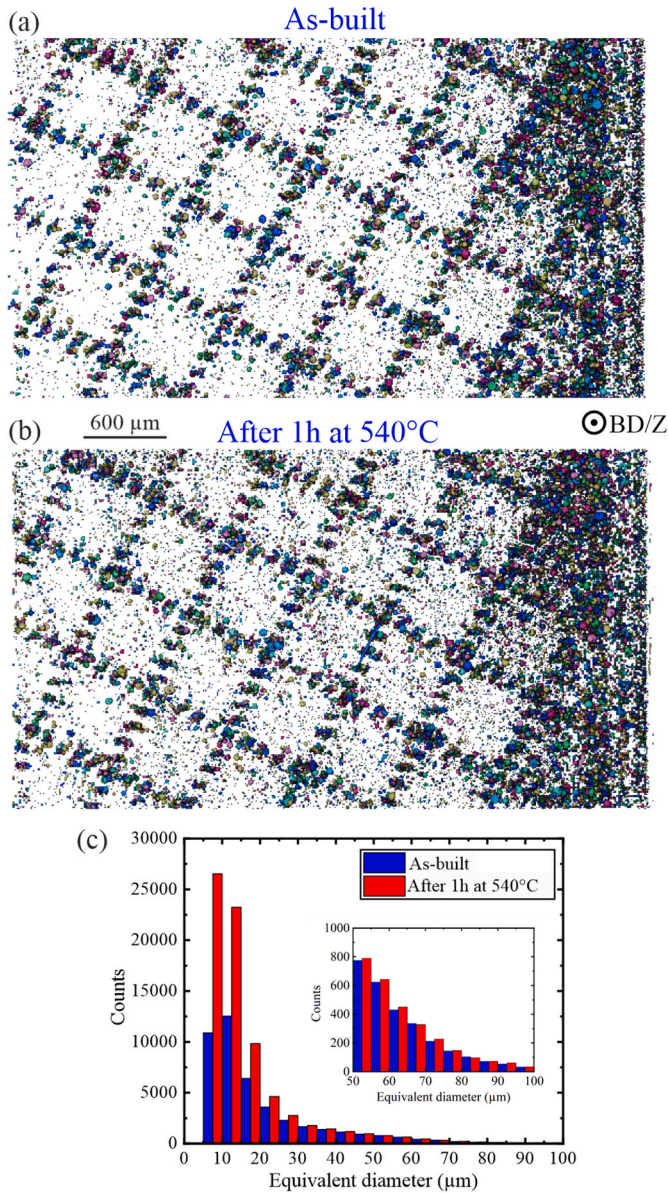
0.52% in the condition after a heat treatment at 540 °C for 1 h. Even though Type I porosity also undergoes size increase, the detected 0.04% increase in porosity mainly results from the TIP-induced size increase of Type II porosity; some small pores are able to reach a size above the detection limit of the tomographic images (>10 μm).

3.3. In-situ heat treatment combined with SXRR

For the sake of simplicity, the analysis of the results obtained with *in-situ* high-temperature SXRR are restricted to a small region, so the porosity size increase as a function of temperature can be clearly shown (Fig. 8a–h). The qualitative evaluation of the size increase is performed using radiographic refraction images of the peak position, whereas the quantitative evaluation is made using the transmission ones (Fig. 8i). Because the flat field is recorded only twice during the heat treatment (see section 2.4.1), some of the artefacts (mostly induced by defects in the CWO scintillator and indicated by red arrows in Fig. 8i) cannot be fully removed. Therefore, noise inevitably influences the quantitative evaluation shown in Fig. 8j. While noise is significant all throughout steps 1 to 12, comparison with Fig. 8a–e indicates that there are no significant changes in pore size and area fraction. Remarkably, the highest porosity increase (~0.013% increase in area fraction) is observed between stages 12 and 13 (Fig. 8f), which corresponds to the ramp-up from 540 °C to 650 °C (these two images have a time delay of ~15 min). Finally, no increase in the area fraction is observed after cooling back to room temperature (compare steps 15 and 16).

Fig. 9 shows the evolution of C_m*d maps as a function of

Fig. 7. 3D volume renderings of laboratory X-ray CT data: (a) of the as-built condition and (b) of the condition after 1 h at 540 °C. (c) Histogram of the spherical equivalent diameter in the two conditions.

values undergo a continuous increase, and the highest values are reached at 650 °C. Surprisingly, the cooling down to room temperature yields even a higher C_m*d mean value than that observed after the last 30 min of heating at 650 °C. Importantly, it is observed that the mean C_m*d increases 60% between the initial and final steps. We consider that the main contribution to the observed increase in the internal specific surface (C_m*d) should correspond to the nucleation and growth of Type II porosity.

The conclusions on porosity growth and evolution of C_m*d mean values are not particular to the local region ($\sim0.7 \times 0.9 \times 1$ mm^3) analysed above and, therefore, can be extrapolated to the entire FoV enabled by the detector ($\sim6.3 \times 4.7 \times 1$ mm^3). In fact, we do not observe any gradients along the building direction, neither of the microstructure nor of the porosity.
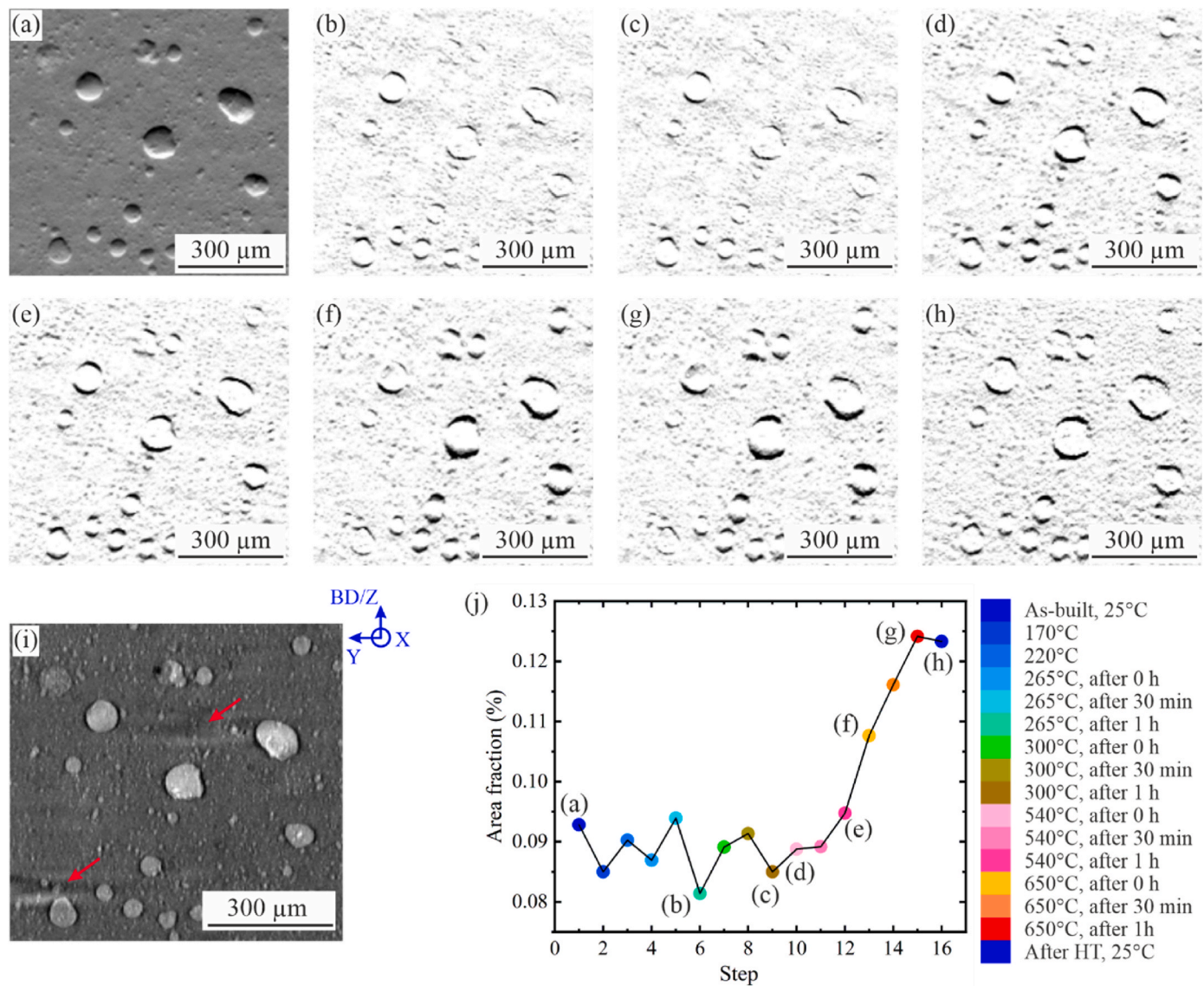
4. Discussion

The observed changes in C_m*d mean values (Fig. 9k) are induced by two different mechanisms: (i) disintegration and spheroidization of the silicon phase, and (ii) thermally induced porosity (TIP).

As introduced in Section 3.1, there are four main stages where the silicon undergoes noticeable morphological changes. These changes induce the C_m*d mean variation observed between room temperature and 300 °C (steps 1 to 10). As shown in Fig. 9k, C_m*d mean values remain stable up to 265 °C; this is in line with literature data [33]. The reduction of C_m*d mean observed at 265 °C after 1 h is induced by the coarsening of the α-Al matrix cells combined with the enlargement of the Si network (*i.e.*, the amount of internal surface is reduced, see Fig. 10a and b). The disintegration of the Si network into particles, starting at 300 °C, leads to vermicular morphologies, consequently increasing C_m*d mean (Fig. 10c); however, C_m*d mean is reduced again when the Si particles transform into rods and start to grow (Fig. 10d). Upon further holding at higher temperatures (540 °C and 650 °C isotherms), C_m*d mean would be expected to decrease due to further coarsening of Si particles (dominated by Ostwald ripening [34]), as well as to the dissolution of Si precipitates back into the α-Al matrix due to the increased Si solubility in this temperature range (Fig. 3f). However, this event is outweighed (in the X-ray refraction signal) by the simultaneous occurrence of porosity growth (TIP).

The physics governing the growth of porosity is complex and a detailed evaluation of this phenomenon is beyond the scope of this work. Nonetheless, it has been reported that, at about 400 °C, the mobility of entrapped hydrogen increases to a level where the internal hydrogen gas pressure can start inducing the porosity increase observed from the beginning of the isotherm at 540 °C (Fig. 10e and f) [29]. This also implies that the advantage of a hydrogen supersaturated α-Al matrix (leading to a reduction of the process-induced hydrogen porosity) can be significantly reduced when performing post-process heat treatment at temperatures higher than $\sim$450 °C [46].

The growth of gas pores as a function of time has been attributed to creep deformation of the surrounding material [48] and is commonly influenced by factors such as the initial pore volume, the dwell time, and the heat-treatment temperature [49]. A logarithmic trend of C_m*d mean values as a function of holding time is observed during 540 °C and 650 °C isotherms (Fig. 9k). Such a behaviour results from the fact that during an isothermal the pressure exerted by the hydrogen decreases as the pore expands, thereby diminishing the driving force available for pore size increase and subsequently reducing the growth rate [49]. Moreover, the pore size increase becomes significantly larger at 650 °C. This is because, in addition to a given increase in hydrogen pressure, the creep rate alsoaround the cavity increases as a function of increasing temperature. Note that the yield strength (YS) of AlSi10Mg at 400 °C is only 6% of that measured at room temperature (YS$_{RT}$ = 240 MPa) [50]. In addition, it is observed that, in both 540 °C and 650 °C isotherms, pores grow faster during the ramping up and early in the isotherms (first 30 min), in agreement with the findings reported in Ref. [36].

temperature. The differences with the results shown in Fig. 8 are substantial: Type I porosity yields crescent-shaped features, for which the C_m*d values vary from about 0.08 to 0.28 in the initial conditions (Fig. 9a), and from 0.17 to 0.3 in the final temperature step (Fig. 9h). The increase of C_m*d values of the background (*i.e.*, from 0.05 to 0.15) is generated by the increase of Type II porosity (induced by both pore growth and nucleation). Also note that the increase of C_m*d is spatially heterogeneous throughout the entire heat treatment cycle (Fig. 9a–h), and the final stage indicates that some regions remain at the original 0.04–0.05 C_m*d values< throughout the entire heating cycle (an example is indicated with a white arrow in Fig. 9h).

The calculation of C_m*d mean values (see examples in Fig. 9i and j) is done using the values of all pixels contained within the region of interest for each temperature step. Such means remain broadly stable at 0.05 in the steps between 1 and 5 (room temperature to 265 °C after 30 min, see Fig. 9k). The mean decreases to 0.04 at steps 6 and 7. However, at step 8 the mean value increases to 0.055, whereas a reduction is observed again at step 9. From 300 °C after 1 h (step 10) forward, the C_m*d mean

Fig. 8. (a) Peak position images recorded at room temperature (25 °C). (b–h) Images showing the results of the subtraction of the image at the temperature step 1 (shown in (a)) from those collected at successive steps: (b) at 265 °C after 1 h, (c) at 300 °C after 1 h, (d) at 540 °C after 0 h, (e) at 540 °C after 1 h, (f) at 650 °C after 0 h, (g) at 650 °C after 1 h, and (h) at room temperature after heat treatment. (i) An example of the transmission images used for the area fraction calculation. Artefacts are indicated with red arrows. (j) Plot of the area fraction against the temperature steps. (For interpretation of the references to colour in this figure legend, the reader is referred to the Web version of this article.)

Interestingly, the growth rate is higher during the cooling (step 16) than during the last half hour of the isotherm at 650 °C (step 15). These results indicate that some other mechanism could contribute to pore growth during cooling. Presumably, pore coalescence coupled with the hydrogen increased solubility in Al at 650 °C (transition to liquidus occurs at 660 °C) could contribute to the drastic deceleration in expansion observed at step 15 (650 °C for 1 h). The subsequent reduction of hydrogen solubility upon cooling would contribute to the greater growth rate observed between steps 15 and 16 (compared to that between steps 14 and 15). Such mechanism would act in combination with the creep deformation still in development because the internal pressure is higher than the yield strength of the material within the 650-400 °C temperature range [29]. Furthermore, the presence of regions with a marginal increase in C_m*d values (indicated with a white arrow in Fig. 9h) might indicate that the Type II pore nucleation and growth occurs heterogeneously at preferential sites [27].

The porosity growth induces a reduction of strength and ductility resulting from the increase of local stress concentration around the pore.

Some authors report that pores smaller than a critical size, which account for a total volumetric porosity of 1%, do not affect the macroscopic behaviour of AM materials in a considerable manner [51]. Early failure of a component is usually induced by the presence of a *killer* defect larger than the critical size [52]. The traditional T6 heat treatment applied to AM AlSi10Mg involves water quenching after the solutionizing step at 500°C–550 °C, which precedes the artificial ageing step at 160–180 °C. Hence, the porosity growth observed in step 16 (Fig. 9h) can be significantly reduced when applying a water quench. Also note that SXRR is useful when evaluating the contour porosity (also called subsurface porosity), which is shown Fig. 4 but cropped out in Fig. 5.

The ripening of Si particles, sketched in Fig. 10, has direct consequences on the static tensile strength and a lot of effort has been dedicated to finding the best combination of properties for each practical application [33,53]. The as-built state possesses the highest fracture (UTS >370 MPa) and yield (YS > 250 MPa) strengths but the lowest ductility (~5%). The stress relief treatments (at 300 °C) leads to a
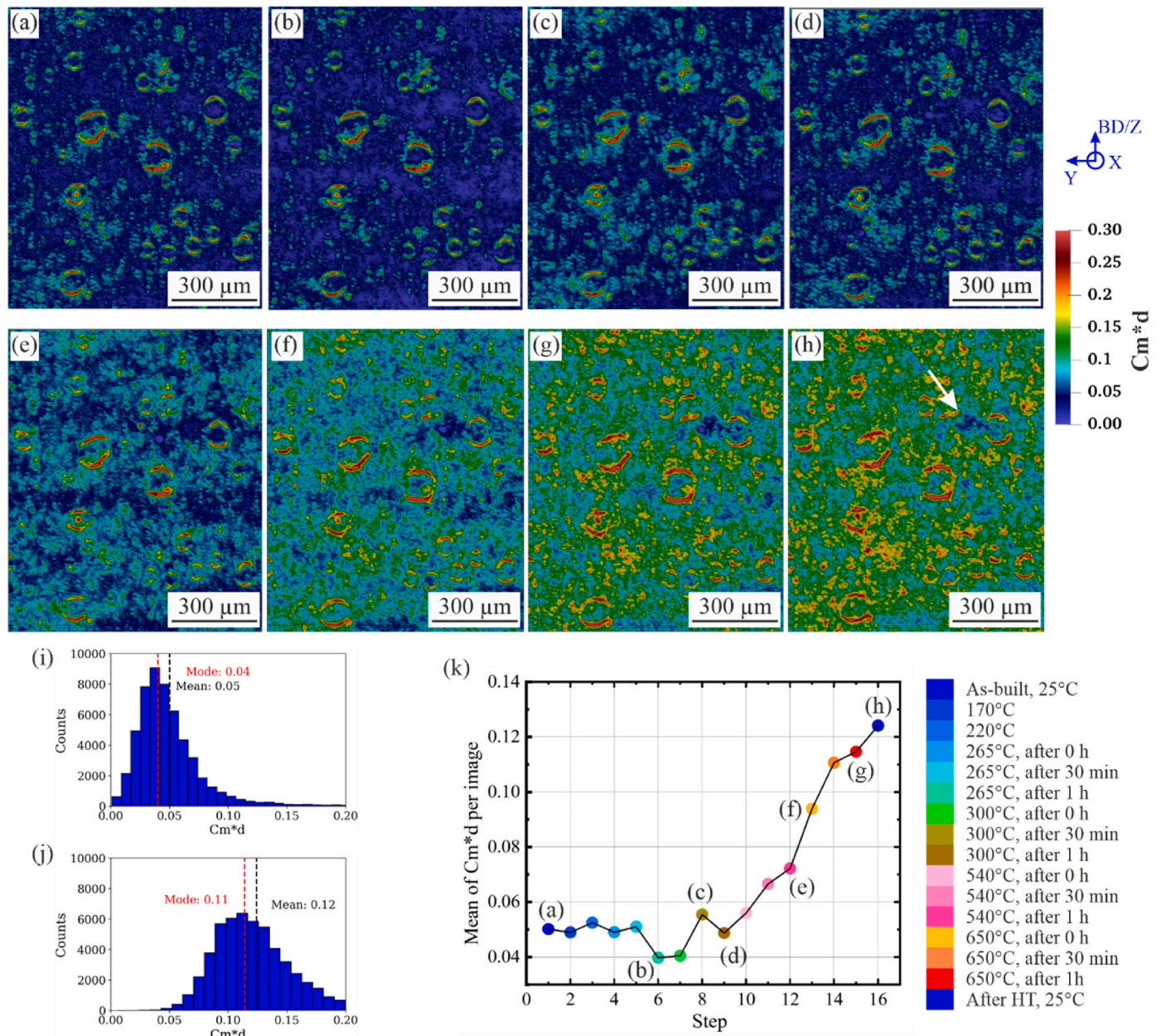
Fig. 9. Colour-coded C_m*d refraction images recorded at (a) room temperature (25 °C), (b) 265 °C after 1 h, (c) 300 °C after 30 min, (d) 300 °C after 1 h, (e) 540 °C after 1 h, (f) 650 °C after 0 h, (g) 650 °C after 1 h, and (h) room temperature after heat treatment. Histograms of the C_m*d values of the image recorded at (i) Step 1 and (j) Step 16. (k) Plot of the mean of C_m*d per image against the temperature steps. (For interpretation of the references to colour in this figure legend, the reader is referred to the Web version of this article.)

reduction of fracture and yield strength (down to about 250 MPa and 200 MPa, respectively), whereas the elongation is increased to ~18% [54]. A solutionizing treatment at 550 °C further lowers the strength (UTS = 170 MPa and YS = 90 MPa) while increasing ductility (24%) [31]. Artificial ageing at 160 °C–180 °C is used to achieve precipitation hardening by the formation of Mg_2Si precipitates. For instance, ageing at 160 °C for 8 h leads to UTS = 240 MPa and YS = 290 MPa (note that these values are usually lower than those of the as-built condition), as well as to a ductility of 9%, which is, nevertheless, higher than that observed in the as-built condition [55].

The visualization of submicron features such as Si particles is commonly performed via techniques such as nano-tomography [56] or focused ion beam (FIB) microscopy [57], but these techniques are limited to relatively small FoVs (*e.g.*, cubic regions of ~200 μm per side) and do not allow statistically sound analyses. The potential of SXRR to detect the thermally-induced evolution of submicron (<5 μm) features over statistically relevant FoVs enabled two major findings: (i) the disintegration of the Si network and subsequent spheroidization is spatially homogeneous, *i.e.*, no differences in the Si precipitation rate are observed along the building direction; and (ii) the porosity growth (mostly Type II) is, on the other hand, spatially heterogenous and most likely favoured at melt pool boundaries. This last point is subject for future research.

5. Conclusions

This work shows how *in-situ* heating coupled with Synchrotron X-ray refraction radiography (SXRR) is a straightforward and robust method for time-resolved (~3–5 min required for a scan) evaluations of thermally induced microstructural changes over macroscopically relevant
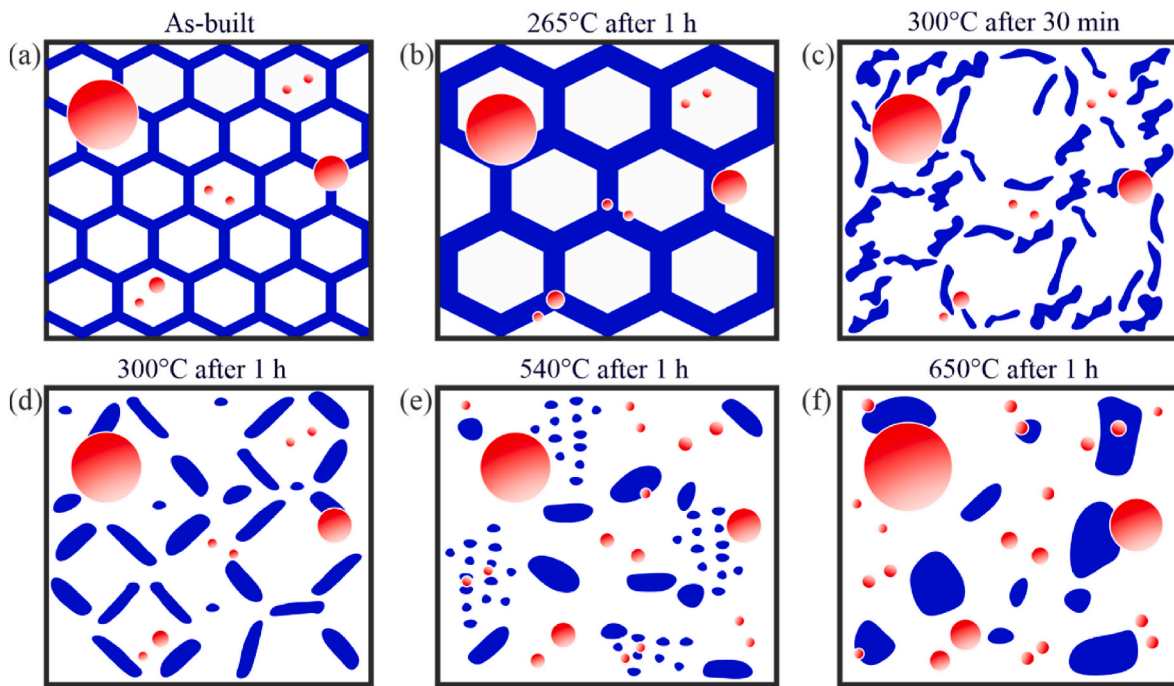
Fig. 10. Schematic illustration of the microstructure and porosity evolution (Si is shown in blue, porosity in red) during heat treatment at (a) room temperature, (b) 265 °C after 1 h, (c) 300 °C after 30 min, (d) 300 °C after 1 h, (e) 540 °C after 1 h, and (f) 650 °C after 1 h. (For interpretation of the references to colour in this figure legend, the reader is referred to the Web version of this article.)

volumes. We studied the effects of *in-situ* heat treatments on both the defect distribution and microstructure of an additively manufactured AlSi10Mg alloy. Our attention was focused on the ripeningm of the eutectic Si network, as well as on the evolution of the thermally-induced porosity (TIP). Through the combination of *in-situ* SXRR, optical microscopy (OM), X-ray computed tomography (XCT), and scanning electron microscopy (SEM) we found that: a) the Si network transforms into spheroidized particles; eventually, only large (a few micrometres) particles remain and the cellular Si structure disappears; b) both large (>10 μm, Type I) and submicron pores (Type II) grow in size during heat treatments, with additional pore nucleation also developing; and c) the decrease of internal specific surface (C_m*d) caused by the futher ripening of polygonal Si particles at 540 °C is superseded by the growth and creation of new pore surfaces.

Thanks to the wide range of monochromatic energies available at the BAM*line* (from 10 to 50 KeV), *in-situ* SXRR can be envisaged for the characterization of many types of materials (*i.e.*, metals, polymers and ceramics) and manufacturing techniques, for which the material performance can be improved by post-processing heat treatments. Moreover, owing to its typically large fields-of-view, SXRR is also well suited for multi-layered and graded materials, where micro-, meso- and macroscopic gradients can be induced during heat treatment.

CRediT authorship contribution statement

Itziar Serrano-Munoz: Conceptualization, Investigation, Visualization, Methodology, Formal analysis, Writing – original draft, Writing – review & editing. **Ilaria Roveda:** Resources, Investigation, Visualization. **Andreas Kupsch:** Investigation, Supervision, Writing – review & editing. **Bernd R. Müller:** Investigation, Supervision, Software. **Giovanni Bruno:** Supervision, Funding acquisition, Writing – review & editing.

Declaration of competing interest

The authors declare that they have no known competing financial interests or personal relationships that could have appeared to influence the work reported in this paper.

Data availability

Datasets related to this article can be obtained upon request to the corresponding author.

Acknowledgements

References

[1] P. Echlin, Handbook of Sample Preparation for Scanning Electron Microscopy and X-Ray Microanalysis, 2009.

[2] E. Beevers, A.D. Brandão, J. Gumpinger, M. Gschweitl, C. Seyfert, P. Hofbauer, T. Rohr, T. Ghidini, Int. J. Fatig. 117 (2018), https://doi.org/10.1016/j.ijfatigue.2018.08.023.

[3] N.O. Larrosa, W. Wang, N. Read, M.H. Loretto, C. Evans, J. Carr, U. Tradowsky, M. M. Attallah, P.J. Withers, Theor. Appl. Fract. Mech. 98 (2018), https://doi.org/10.1016/j.tafmec.2018.09.011.

[4] G. Kasperovich, J. Haubrich, J. Gussone, G. Requena, Mater. Des. 105 (2016), https://doi.org/10.1016/j.matdes.2016.05.070.

[5] M.P. Hentschel, R. Hosemann, A. Lange, B. Uther, R. Bruckner, Acta Crystallogr. A 43 (1987), https://doi.org/10.1107/S0108767387099100.

[6] B.R. Muller, A. Lange, M. Harwardt, M.P. Hentschel, Refraction enhanced micro-CT for non-destructive materials characterization, in: 2008 Ieee Nuclear Science Symposium and Medical Imaging Conference (2008 Nss/Mic), 1-9, 2009, pp. 5438–5443.

[7] B.R. Müller, A. Lange, M. Harwardt, M.P. Hentschel, Adv. Eng. Mater. 11 (2009), https://doi.org/10.1002/adem.200800346.

[8] B.R. Müller, R.C. Cooper, A. Lange, A. Kupsch, M. Wheeler, M.P. Hentschel, A. Staude, A. Pandey, A. Shyam, G. Bruno, Acta Mater. 144 (2018), https://doi.org/10.1016/j.actamat.2017.10.030.

[9] A. Kupsch, A. Lange, M.P. Hentschel, Y. Onel, T. Wolk, A. Staude, K. Ehrig, B. R. Müller, G. Bruno, J. Ceram. Sci. Technol. 4 (2013), https://doi.org/10.4416/JCST2013-00021.

[10] A. Kupsch, R. Laquai, B.R. Muller, S. Paciornik, J. Horvath, K. Tushtev, K. Rezwan, G. Bruno, Adv. Eng. Mater. (2021), https://doi.org/10.1002/adem.202100763.

[11] J. Nellesen, R. Laquai, B.R. Müller, A. Kupsch, M.P. Hentschel, N.B. Anar, E. Soppa, W. Tillmann, G. Bruno, J. Mater. Sci. 53 (2018), https://doi.org/10.1007/s10853-017-1957-x.

[12] A. Kupsch, V. Trappe, B.R. Müller, G. Bruno, IOP Conf. Ser. Mater. Sci. Eng. 942 (2020), https://doi.org/10.1088/1757-899x/942/1/012035.

[13] R. Laquai, B. Müller, G. Kasperovich, G. Requena, J. Haubrich, G. Bruno, Mater. Perform. Char. 9 (2020), https://doi.org/10.1520/MPC20190080.

[14] R. Laquai, B.R. Müller, G. Kasperovich, J. Haubrich, G. Requena, G. Bruno, Mater. Res. Lett. 6 (2018), https://doi.org/10.1080/21663831.2017.1409288.

[15] R. Laquai, B.R. Müller, J.A. Schneider, A. Kupsch, G. Bruno, Metall. Mater. Trans. 51 (2020), https://doi.org/10.1007/s11661-020-05847-5.

[16] M.K. Thompson, G. Moroni, T. Vaneker, G. Fadel, R.I. Campbell, I. Gibson, A. Bernard, J. Schulz, P. Graf, B. Ahuja, F. Martina, CIRP Ann. 65 (2016), https://doi.org/10.1016/j.cirp.2016.05.004.

[17] I. Polmear, D. StJohn, J.F. Nie, M. Qian, Light Alloys: Metallurgy of the Light Metals, Elsevier Science, 2017.

[18] K.V. Yang, P. Rometsch, T. Jarvis, J. Rao, S. Cao, C. Davies, X. Wu, Mater. Sci. Eng.: A 712 (2018), https://doi.org/10.1016/j.msea.2017.11.078.

[19] S. Tammas-Williams, H. Zhao, F. Léonard, F. Derguti, I. Todd, P.B. Prangnell, Mater. Char. 102 (2015), https://doi.org/10.1016/j.matchar.2015.02.008.

[20] M.J. Paul, Q. Liu, J.P. Best, X. Li, J.J. Kruzic, U. Ramamurty, B. Gludovatz, Acta Mater. (2021) 211, https://doi.org/10.1016/j.actamat.2021.116869.

[21] Z.H. Xiong, S.L. Liu, S.F. Li, Y. Shi, Y.F. Yang, R.D.K. Misra, Mater. Sci. Eng.: A (2019) 740–741, https://doi.org/10.1016/j.msea.2018.10.083.

[22] I. Rosenthal, R. Shneck, A. Stern, Mater. Sci. Eng.: A 729 (2018), https://doi.org/10.1016/j.msea.2018.05.074.

[23] N.T. Aboulkhair, N.M. Everitt, I. Ashcroft, C. Tuck, Additive Manufacturing, 2014, pp. 1–4, https://doi.org/10.1016/j.addma.2014.08.001.

[24] N. Read, W. Wang, K. Essa, M.M. Attallah, Mater. Des. 65 (2015), https://doi.org/10.1016/j.matdes.2014.09.044.

[25] C. Weingarten, D. Buchbinder, N. Pirch, W. Meiners, K. Wissenbach, R. Poprawe, J. Mater. Process. Technol. 221 (2015), https://doi.org/10.1016/j.jmatprotec.2015.02.013.

[26] A.A. Martin, N.P. Calta, S.A. Khairallah, J. Wang, P.J. Depond, A.Y. Fong, V. Thampy, G.M. Guss, A.M. Kiss, K.H. Stone, C.J. Tassone, J. Nelson Weker, M. F. Toney, T. van Buuren, M.J. Matthews, Nat. Commun. 10 (2019), https://doi.org/10.1038/s41467-019-10009-2.

[27] H. Toda, T. Hidaka, M. Kobayashi, K. Uesugi, A. Takeuchi, K. Horikawa, Acta Mater. 57 (2009), https://doi.org/10.1016/j.actamat.2009.01.026.

[28] X.P. Li, K.M. O'Donnell, T.B. Sercombe, Addit. Manuf. 10 (2016), https://doi.org/10.1016/j.addma.2016.01.003.

[29] E. Strumza, S. Hayun, S. Barzilai, Y. Finkelstein, R. Ben David, O. Yeheskel, J. Mater. Sci. 54 (2019), https://doi.org/10.1007/s10853-019-03452-5.

[30] D.E.J. Talbot, Int. Metall. Rev. 20 (1975), https://doi.org/10.1179/imtlr.1975.20.1.166.

[31] W. Li, S. Li, J. Liu, A. Zhang, Y. Zhou, Q. Wei, C. Yan, Y. Shi, Mater. Sci. Eng.: A 663 (2016), https://doi.org/10.1016/j.msea.2016.03.088.

[32] K.G. Prashanth, S. Scudino, J. Eckert, Acta Mater. 126 (2017), https://doi.org/10.1016/j.actamat.2016.12.044.

[33] J. Fiocchi, A. Tuissi, C.A. Biffi, Mater. Des. 204 (2021), https://doi.org/10.1016/j.matdes.2021.109651.

[34] P. Van Cauwenbergh, V. Samaee, L. Thijs, J. Nejezchlebová, P. Sedlák, A. Iveković, D. Schryvers, B. Van Hooreweder, K. Vanmeensel, Sci. Rep. 11 (2021), https://doi.org/10.1038/s41598-021-85047-2.

[35] F. Bosio, H. Shen, Y. Liu, M. Lombardi, P. Rometsch, X. Wu, Y. Zhu, A. Huang, JOM (J. Occup. Med.) 73 (2021), https://doi.org/10.1007/s11837-020-04523-8.

[36]] INVALID CITATION !!! .

[37] F. Wilde, M. Ogurreck, I. Greving, J.U. Hammel, F. Beckmann, A. Hipp, L. Lottermoser, I. Khokhriakov, P. Lytaev, T. Dose, H. Burmester, M. Müller, A. Schreyer, AIP Conf. Proc. 1741 (2016), https://doi.org/10.1063/1.4952858.

[38] Avizo Software, Last accessed in August 2021, https://www.fei.com/software/avizo3d/%C2%A0#gsc.tab=0.

[39] A. Rack, S. Zabler, B.R. Müller, H. Riesemeier, G. Weidemann, A. Lange, J. Goebbels, M. Hentschel, W. Görner, Nuclear instruments and methods in physics research section A: accelerators, Spectrometers, Detect. Assoc. Equip. (2008) 586, https://doi.org/10.1016/j.nima.2007.11.020.

[40] W. Görner, M.P. Hentschel, B.R. Müller, H. Riesemeier, M. Krumrey, G. Ulm, W. Diete, U. Klein, R. Frahm, Nuclear instruments and methods in physics research section A: accelerators, Spectrometers, Detect. Assoc. Equip. (2001) 467–468, https://doi.org/10.1016/S0168-9002(01)00466-1.

[41] A. Lange, M.P. Hentschel, A. Kupsch, B.R. Müller, Int. J. Mater. Res. 103 (2012), https://doi.org/10.3139/146.110659.

[42] A.M. Al-Falahat, A. Kupsch, M.P. Hentschel, A. Lange, N. Kardjilov, H. Markötter, I. Manke, Rev. Sci. Instrum. 90 (2019), https://doi.org/10.1063/1.5097170.

[43] D. Chapman, W. Thomlinson, R.E. Johnston, D. Washburn, E. Pisano, N. Gmür, Z. Zhong, R. Menk, F. Arfelli, D. Sayers, Phys. Med. Biol. 42 (1997), https://doi.org/10.1088/0031-9155/42/11/001.

[44] D. Mani, A. Kupsch, B.R. Müller, J. Balko, G. Bruno, Diffraction Enhanced Imaging analysis with PesudoVoigt1 fit function, 2022 in preparation.

[45] V.R. G, D.J. FL, Python Reference Manual, Centrum voor Wiskunde en Informatica Amsterdam, 1995. https://www.python.org/.

[46] P. Van Cauwenbergh, G.K. Muralidharan, P. Bigot, L. Thijs, B. Hooreweder, K. Vanmeensel, Reducing hydrogen pores and blisters by novel strategies and tailored heat, Treat. Laser Powder Bed Fusion AlSi7Mg0 6 (2019).

[47] E. Louvis, P. Fox, C.J. Sutcliffe, J. Mater. Process. Technol. 211 (2011), https://doi.org/10.1016/j.jmatprotec.2010.09.019.

[48] N.G.D. Murray, D.C. Dunand, Acta Mater. 52 (2004), https://doi.org/10.1016/j.actamat.2004.01.039.

[49] S. Tammas-Williams, P.J. Withers, I. Todd, P.B. Prangnell, Scripta Mater. 122 (2016), https://doi.org/10.1016/j.scriptamat.2016.05.002.

[50] N.E. Uzan, R. Shneck, O. Yeheskel, N. Frage, Addit. Manuf. 24 (2018), https://doi.org/10.1016/j.addma.2018.09.033.

[51] A. du Plessis, I. Yadroitsava, I. Yadroitsev, Mater. Des. 187 (2020), https://doi.org/10.1016/j.matdes.2019.108385.

[52] S. Tammas-Williams, P.J. Withers, I. Todd, P.B. Prangnell, Sci. Rep. 7 (2017), https://doi.org/10.1038/s41598-017-06504-5.

[53] E. Padovano, C. Badini, A. Pantarelli, F. Gili, F. D'Aiuto, J. Alloys Compd. 831 (2020), https://doi.org/10.1016/j.jallcom.2020.154822.

[54] N.E. Uzan, R. Shneck, O. Yeheskel, N. Frage, Mater. Sci. Eng.: A 704 (2017), https://doi.org/10.1016/j.msea.2017.08.027.

[55] M. Pellizzari, M. Malfatti, C. Lora, F. Deirmina, BHM Berg- Hüttenmännische Monatsh. 165 (2020), https://doi.org/10.1007/s00501-020-00956-5.

[56] J. Villanova, R. Daudin, P. Lhuissier, D. Jauffrès, S. Lou, C.L. Martin, S. Labouré, R. Tucoulou, G. Martínez-Criado, L. Salvo, Mater. Today 20 (2017), https://doi.org/10.1016/j.mattod.2017.06.001.

[57] J.G. Santos Macías, T. Douillard, L. Zhao, E. Maire, G. Pyka, A. Simar, Acta Mater. 201 (2020), https://doi.org/10.1016/j.actamat.2020.10.001.